https://doi.org/10.1038/s44306-025-00092-1

Time multiplexed single node reservoir computing enabled by transient photon magnon coupling

Haechan Jeon[1,3], Bojong Kim[1,3], Loïc Millet[1,2,3] & Sang-Koog Kim[1,3] ✉

We present a reservoir computing system that utilizes the transient dynamics of photon-magnon coupling (PMC) for high-accuracy temporal data processing, specifically spoken-digit recognition, while minimizing hardware resources. By time-multiplexing a single physical node into ten virtual nodes, our approach achieves 89% classification accuracy, comparable to conventional systems using hundreds or thousands of nodes. This hardware-efficient design preserves the rich nonlinear dynamics essential for temporal processing while significantly reducing energy consumption. In addition, the inter-node connectivity derived from the transient response of PMC requires that the total sampling duration remains below the PMC decay time, and that the pulse interval be sufficiently small to enable overlapping oscillations for effective time-multiplexed reservoir operation. Our results demonstrate that this transient PMC approach can enable scalable, low-power neuromorphic computing for IoT devices, real-time edge computing, and other resource-constrained environments.

Neuromorphic computing, inspired by the structure and function of the human brain, aims to develop artificial systems capable of efficient, adaptive information processing with low power consumption[1,2]. Within this field, reservoir computing (RC) has attracted considerable attention due to its ability to effectively handle temporal data by exploiting the intrinsic dynamics of complex systems[3]. In a typical RC scheme comprising an input layer, a dynamic reservoir that maps input signals into a high-dimensional state space, and a readout layer, temporal dependencies are effectively captured[4], making it particularly suitable for tasks such as time-series prediction, pattern recognition, and classification.

A wide range of physical RC implementations have been explored, including photonic systems[5–10], memristive devices[11–16], and spintronic platforms[17–25]. Among these, spintronic approaches offer low power consumption, nanoscale integration, and robust parallel processing, thus aligning well with the requirements of neuromorphic applications[26]. In spintronic systems, the utilization of transient dynamics can allow for computational efficiency and scalability.

Recently, the transient dynamics of photon-magnon coupling (PMC) have emerged as a promising mechanism for RC[27]. Here, magnons (quanta of spin waves) interact with cavity-confined microwave photons to form cavity magnon-polariton states (CMP) that naturally provide the nonlinear dynamic behavior essential for temporal data processing[26]. Our prior PMC-based RC study focused on steady-state dynamics[28], which prevented the implementation of short-term memory and required complex and slow hardware for information encoding. In contrast, utilizing transient responses of PMC[29,30] can enhance both the versatility and accuracy of RC systems[31]. By operating in transient regimes, one can more effectively capture fast temporal features while simultaneously simplifying the underlying hardware.

Here, we report an RC system that employs the transient response of PMC to process temporal data efficiently and accurately. By time-multiplexing a single physical node into multiple virtual nodes[5,32] and carefully optimizing parameters such as the virtual node interval ($\Delta\tau$) and the number of virtual nodes (N), we establish the temporal correlations between nodes needed for short-term memory without requiring additional hardware[33,34]. Indeed, the intrinsic decay time (τ_{CMP}) of cavity magnon-polaritons must be sufficiently long to accommodate the chosen total sampling duration ($\tau = \Delta\tau \times N$), ensuring that transient oscillations do not vanish prematurely; likewise, the pulse interval (δ) must remain small enough for overlapping transient states, thereby strengthening inter-node connectivity and supporting robust time-multiplexed reservoir operation.

To validate our approach, we perform spoken-digit recognition, a benchmark temporal classification task. Our system achieved ~89% accuracy using only one physical node time-multiplexed into ten virtual nodes, comparable to conventional RC systems employing hundreds or thousands of nodes. This balance between hardware simplicity and robust performance indicates the potential of transient PMC-based RC for scalable, low-

[1]National Creative Research Initiative Center for Spin Dynamics and Spin-Wave Devices, Nanospinics Laboratory, Research Institute of Advanced Materials, Department of Materials Science and Engineering, Seoul National University, Seoul, 08826, South Korea. [2]Present address: Group of Applied Physics, University of Geneva, Geneva, Switzerland. [3]These authors contributed equally: Haechan Jeon, Bojong Kim, Loïc Millet, Sang-Koog Kim. ✉e-mail: sangkoog@snu.ac.kr

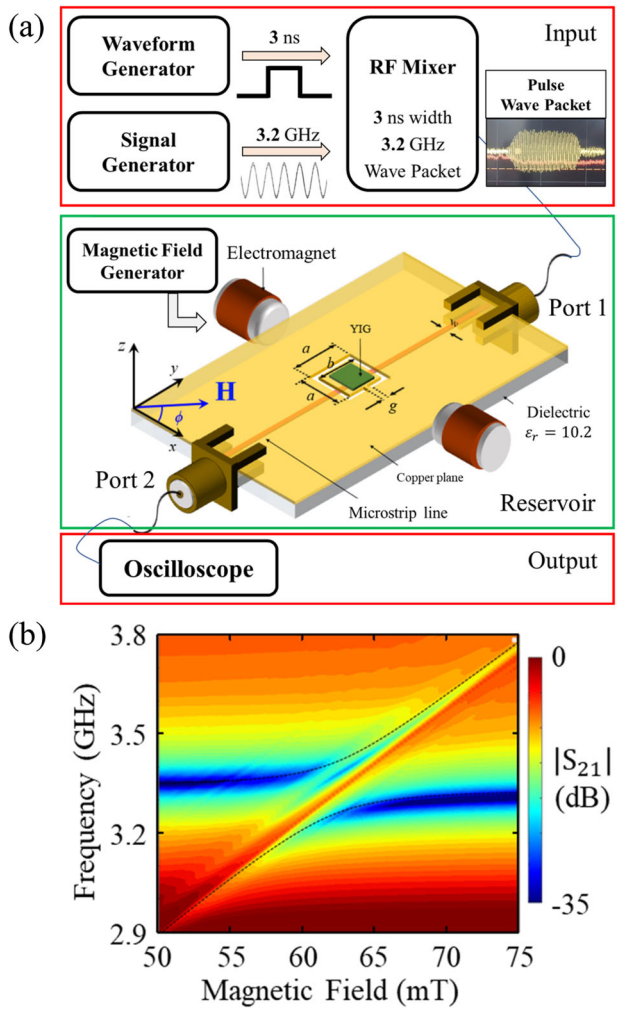

Fig. 1 | Experimental setup for transient measurement and steady-state signature of PMC. a Schematic of the experimental setup for capturing transient measurement in the PMC hybrid system. The input signal, generated by waveform and RF signal generators, is mixed to form a pulse wave packet, and transmits into the hybrid ISRR-YIG system. (see "Methods" for device dimensions). **b** Experimentally measured $|S_{21}|$ as a function of microwave frequency and applied magnetic field (*f*-*H* plane), illustrating the characteristic anti-crossing behavior of the PMC system.

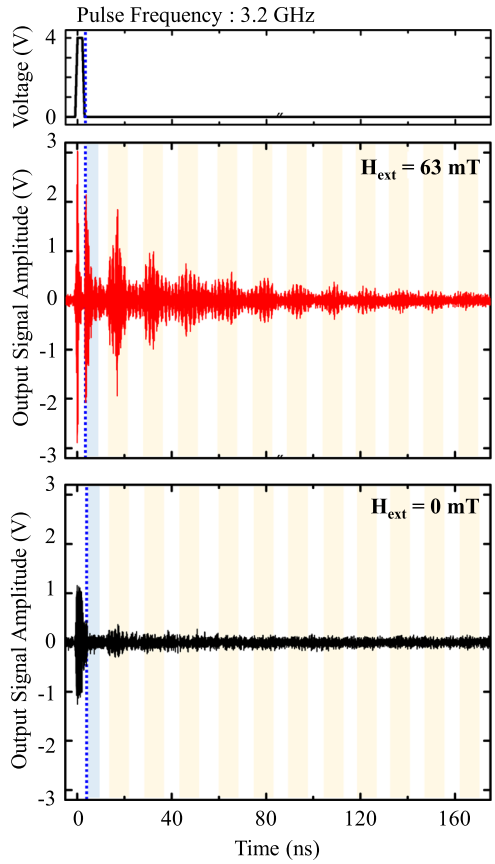

Fig. 2 | Transient response of the PMC hybrid system. The red trace (H_{ext} = 63 mT) exhibits sustained oscillations extending beyond the initial pulse-induced oscillations (blue-shaded region). In contrast, the black trace (H_{ext} = 0 mT) shows rapid signal decay. The beige-shaded region indicates the prolonged oscillation resulting from PMC.

power neuromorphic computing, with particular relevance for resource-constrained scenarios such as IoT devices and real-time edge computing.

Results

Photon-Magnon Coupling in YIG/ISRR Hybrid System

Our experimental setup for investigating transient PMC response is illustrated in Fig. 1a. The hybrid sample consist of an inverted split-ring resonator (ISRR) coupled to a thin yttrium iron garnet (YIG) film[35]. We measured the scattering parameter ($|S_{21}|$) using a Vector Network Analyzer (VNA), sending RF signals through port 1 of the microstrip line and detecting the output at port 2 in the frequency domain. A static magnetic field was applied in-plane at an angle $\phi = 33°$ perpendicular to the microstrip axis, chosen to suppress higher-order spin-wave modes and optimize the ferromagnetic resonance (FMR) by avoiding complex PMC results caused by these higher-order modes[36] (see ref. 36 for details).

Figure 1b illustrates the characteristic anticrossing of magnon-photon coupled modes in the ISRR/YIG hybrid system, illustrating coherent coupling between individual photon and magnon excitations. As the FMR mode's frequency approached the photon mode, they exhibited anticrossing behavior (see Supplementary Fig. 1), repelling each other to form cavity-magnon polaritons[35,37], confirming strong, coherent PMC coupling, as shown in Fig. 1b. To understand the anticrossing dispersion observed in Fig. 1b, we considered a simplified analytical model to describe the dispersion relation in the anticrossing regime. In our experiment, the damping parameters were estimated as $\alpha = 3.2 \times 10^{-4}$ for the magnon (YIG) and $\beta = 2.3 \times 10^{-2}$ for the photon (ISRR) mode (see Supplementary Figs. 2 and 3 for details). An approximate solution for the hybrid eigenfrequencies is given by the analytical expression in ref. 35:

$$\omega_{\pm} = \frac{\omega_p + \omega_m}{2} \pm \sqrt{g^2 + \left(\frac{\omega_p - \omega_m}{2}\right)^2}, \quad (1)$$

where ω_p and ω_m are the eigenfrequency of the photon and magnon modes, respectively, and g is the coupling strength. By fitting Eq. (1) to the $|S_{21}|$ spectra, we estimate the coupling strength $g/2\pi = 70$ MHz, consistent with the calculated result in Supplementary Fig. 3d. This pronounced anticrossing and the resulting hybrid modes in the PMC regime are central to the generation of the nonlinear state spaces required for RC operations[35,37].

Transient Response of Coherent Photon-Magnon Coupling

Figure 2 illustrates the PMC hybrid system's transient response versus time under the conditions of pulsed wave packet (a mixture of pulse and sinusoidal waves), as shown in the top box of Fig. 1a. We compared the coupled and uncoupled cases under an input signal of a 3 ns-width pulse including 3.20 GHz oscillation at an external magnetic field of 63 mT (ω_m = 3.2 GHz). This frequency-field configuration was chosen to effectively explore the nonlinear dynamics arising from PMC[29,30]. The red-color oscillations (active PMC at H_{ext} = 63 mT), as shown in Fig. 2, differ markedly from the black-color oscillations (no coupling at H_{ext} = 0 mT), where the oscillation signal

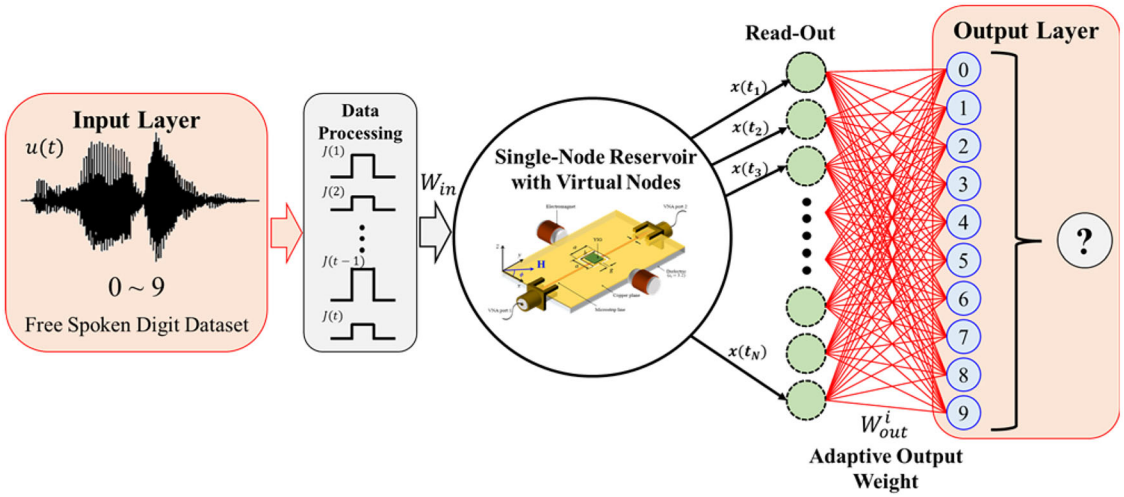

Fig. 3 | Schematic representation of the time-multiplexed reservoir computing framework employed for spoken digit recognition. Input spoken digits from 0 to 9 are processed through time-multiplexing within a single physical node to create multiple virtual nodes. The resulting high-dimensional state space supports efficient temporal data classification in an output layer. Each virtual node $x_i(t)$ corresponds to a transient response sampled at $t + i\Delta\tau$, as used in Eq. (3).

decays almost fully after about 5 ns, leaving minimal residual oscillations. To investigate how the input frequency, coupling strength, and pulse width manifest in the spectral response, we conducted a frequency-domain analysis of the transient signal (see Supplementary Fig. 4). These residual oscillations at $H_{ext} = 0$ mT are purely photonic and are unrelated to spin-wave excitations, which require a finite bias field. In contrast, under PMC, oscillations persist well even beyond the initial 3 ns pulse with no subsequent external excitation, reflecting the sustained energy exchange between magnon and photon modes. Time-resolved measurements reveal clear Rabi oscillations with a coupling strength of $g/2\pi = 70$ MHz, corresponding to an oscillation period of $t_R = 2\pi/g = 14.3$ ns. The system retains a coherent state for $\tau_{CMP} = 40$ ns following the trailing edge of the input pulse, defining a short-term memory window (Fig. 2, middle panel). This persistence is governed by the finite decay time τ_{CMP} of the cavity magnon-polaritons, which effectively serves as a form of short-term memory by retaining a coherent oscillatory state without further input. In our setup, the frequency mixing partly arises from the measurement process: using an RF mixer to acquire the transient response combines multiple frequency components, revealing otherwise hidden oscillations (see "Method").

We note that there are two key requirements for effective RC: (1) a nonlinear response to inputs, and (2) sufficient memory to capture temporal dependencies. In our hybrid system, the coupled-mode oscillation amplitude depends nonlinearly on the input pulse voltage (see Supplementary Fig. 5), while the sustained oscillation in Fig. 2 provides enough short-term memory for tackling time-series classification tasks in RC. Indeed, in typical time-delay RC, delayed feedback loops establish a long-term memory by feeding a node's past output as an input[32], which complements other short-term memory mechanisms. In contrast, our system does not strongly implement such feedback loops, as the CMP decay time is comparable to the chosen total sampling duration ($\tau_{CMP} \approx \tau = N \times \Delta\tau(\text{ns}) = 10 \times 4.0 = 40$ ns). Instead, the periodic oscillations effectively maintain temporal correlations to ensure that an intrinsic short temporal memory mechanism operates within τ_{CMP}.

This intrinsic short temporal memory is especially advantageous for temporal tasks like spoken-digit recognition and NARMA10[38]. In particular, spoken-digit recognition is a benchmark temporal classification problem, dealing with the process of time-dependent audio signals. It underpins many voice-based applications (e.g., automated call routing and various human-computer interactions) and involves transforming raw audio signals into discrete numeric classes. RC is well-suited for such tasks due to its inherent ability to manage time-dependent input data. In this study, we employ the widely adopted Free-Spoken Digit Dataset (FSDD) by Zohar Jackson[39], which provides diverse audio samples from multiple speakers, supporting robust generalization across various pronunciations and accents.

Time-Multiplexed Reservoir Computing

Figure 3 illustrates a schematic of the time-multiplexed reservoir computing framework employed in this study for spoken digit recognition. In this approach, a single physical node is expanded into multiple virtual nodes (dotted circles) through time multiplexing, thus substantially reducing hardware complexity[40]. Processing begins with an input layer that receives raw spoken-digit signals $J(t)$ for digits 0, 1, 2, …., and 9. These signals are transformed through a time-multiplexing step and segmented over an interval $\Delta\tau$. Then, a random mask matrix is applied per segment (see Supplementary Figs. 7 and 8), which defines the weights from the input layer to the reservoir W^{in}. These transformed, segmented signals are sequentially fed to the physical node, which allows the single physical node to emulate a chosen number of virtual nodes, thus defining the reservoir dimension. Owing to the cavity magnon-polariton-induced short-term memory, neighboring nodes are dependent. These inter-node connections are key to capturing temporal dependencies and are strongly regulated by the time interval $\Delta\tau$.

Although traditional delay-based RC does not strictly require τ to be shorter than the node's intrinsic response time[5], our PMC reservoir behaves differently. Here, strong photon–magnon hybridization gives rise to Rabi-like oscillations and periodic energy exchange between the two modes, with a characteristic decay time $\tau_{CMP} \sim 40$ ns, which delineates the interval over which coherent oscillations persist. If τ significantly exceeds this decay time, the hybrid modes decohere and the system transitions into a weakly coupled regime, diminishing its ability to preserve temporal dependence. Our experiments support that increasing τ beyond the decay interval by expanding the virtual node count N under a fixed node spacing $\Delta\tau$ degrades RC performance. Consequently, maintaining τ within the hybrid mode's decay timescale is crucial for optimal PMC-based RC.

In Fig. 3, the output layer maps the high-dimensional reservoir states to the final classification output, which in this study represents digits 0 ~ 9. During training, the output weights w^i_{out} are adjusted to minimize prediction errors, thereby learning an optimal mapping from reservoir states to desired labels. The final output is thus computed as:

$$y(t) = \sum_{i=1}^{N} w^i_{\text{out}} x_i(t), \tag{2}$$

In this expression, $x_i(t)$ denotes the transient response at the i-th virtual node, corresponding to the input sampled at $t + i\Delta\tau$, where $\Delta\tau$ is the time interval between virtual nodes, and i ∈ [1, N]. This formulation captures the time-multiplexed readout of the reservoir within a total sampling duration defined by $\tau = N \times \Delta\tau$. The output $y(t)$ thus reflects the integration of short-term temporal memory encoded across all virtual nodes without invoking a physical delay line.

Figure 4 shows the signal processing workflow and readout mechanism in our physical RC system, detailing how the transient output from the single-node reservoir (Fig. 3) is transformed for an effective machine-learning application. Indeed, the raw transient signal is inherently noisy and contains multiple high-frequencies components, which can hinder direct application of machine-learning algorithms. To address this, we employed a three-step signal processing approach adapted from ref. [22]. First, as shown in Fig. 4b, we performed envelope detection to extract the amplitude variations of the RF signal. This step preserves the essential temporal information while attenuating the dominant 3.20 GHz frequency component and other high-frequency noise. Next, we applied a low-pass filtering with a 1 GHz cutoff frequency. Frequencies above 1 GHz mainly consist of mixed signals arising from the high-frequency input pulse (3.20 GHz) and coupling-related components (~70–80 MHz), which contribute negligible information to the learning process. This filtering step reduces high-frequency content by over 10 dB, lowering overall noise by about 60% and resulting in a more interpretable waveform.

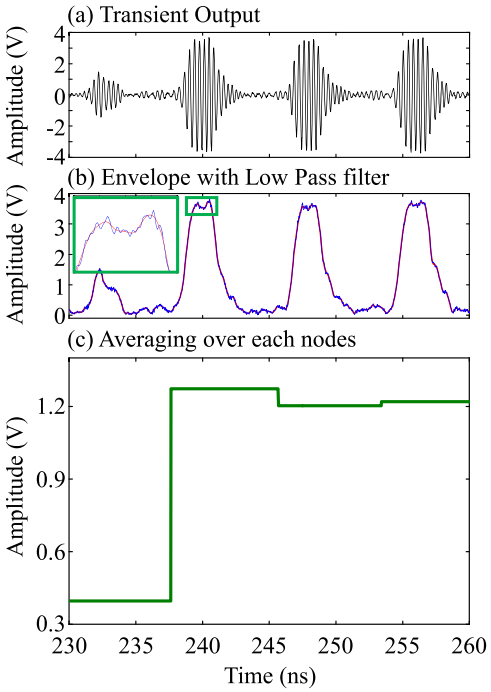

Fig. 4 | Readout extraction from transient PMC response. a Measured transient output response captured by a high-resolution oscilloscope, including mixed frequency components and noise. **b** Raw transient signal (blue) and its processed form (red) after envelope detection and low-pass filtering (cutoff at 1 GHz) to reduce high-frequency noise and enhance essential temporal features. **c** Readout values, representing each virtual node's state, are derived from the filtered signals, forming the input for the machine learning-based classification.

Finally, after low-pass filtering, we averaged the signal over each time-multiplexed segment of duration $\Delta\tau$ [see Fig. 4c], generating a stable readout value x. These readout values x are then combined with the output weight matrix W_{out} to generate the classification output y. We trained W_{out} using logistic regression, which is well-suited for classification tasks[41] (e.g., spoken-digit recognition), due to its capacity for multi-class discrimination even in nonlinear feature space. Iterative updates of W_{out} further balance learning speed and accuracy, ensuring a robust final model.

Figure 5a presents our RC system's classification accuracy as a function of the number of test classes. The system attains 89% accuracy when tested on 100 spoken-digit samples, demonstrating its ability to generalize as data diversity increases. As the number of test samples increases from 70 to 100, accuracy improves by approximately 12%, indicating more diverse datasets better capture input variability. After reaching 100 test samples, the standard deviation (~3.5%) remains relatively low, confirming stable performance across multiple samples.

Figure 5b shows the accuracy as a function of training iterations. Fewer than 30 iterations result in accuracy below 65%, indicating underfitting and limited pattern learning. By 80 iterations, accuracy peaks at 89%, with a confidence interval of ±2%, signifying stable learning and effective generalization. Beyond 80 iterations, accuracy declines to about 83% at 100 iterations, which evidence that the model begins to memorize the training data rather than generalize from it, a common characteristic of overfitting[42,43]. To clarify the subtle changes in accuracy post-80 iterations, we introduced grid lines in Fig. 5b, highlighting a small (2–3%) but consistent decline. Multiple runs confirm that this dip is reproducible,

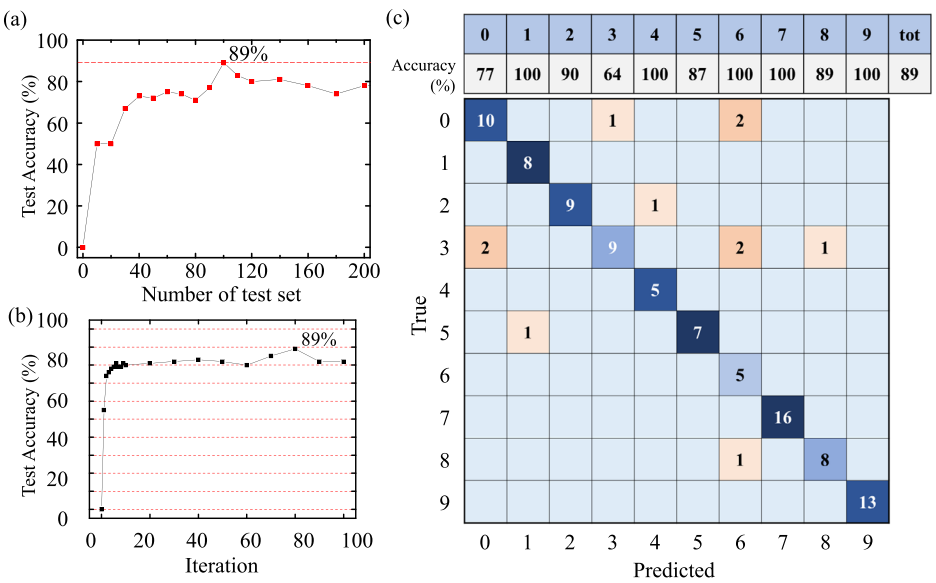

Fig. 5 | Evaluation of spoken-digit classification accuracy. a Test accuracy as a function of the number of test classes. Accuracy reaches 89% at 100 test samples. **b** Test accuracy versus iteration count. Accuracy peaks at 89% after 80 iterations before declining due to overfitting. **c** Confusion matrix illustrates classification performance across all digits.

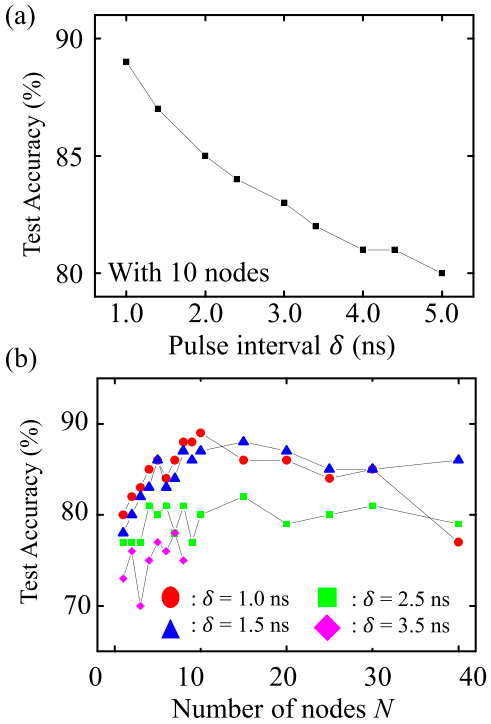

Fig. 6 | Classification accuracy dependence on pulse interval and number of nodes. a Test accuracy as function of the pulse interval δ, with the number of nodes fixed at $N = 10$. **b** Test accuracy as a function of N for three pulse intervals (red circles for 1.0 ns, blue triangles for 1.5 ns, green squares for 2.5 ns, and magenta diamonds for 3.5 ns).

highlighting the trade-off between adequate training and overfitting in our reservoir system.

Figure 5c shows a confusion matrix, a widely used tool for evaluating classification tasks. The x-axis represents predicted digits, and the y-axis denotes true digits. Each cell quantifies how many instances of a given digit fall into each predicted category. Dark-blue diagonal cells mark correct classifications, while transitioning toward orange indicates increasing misclassifications rates. Overall, the system distinguishes digits with clearly distinct acoustic patterns quite well. For instance, "1," "4," "6," "7," and "9" achieve 100% recognition, demonstrating the model's proficiency in isolating unique frequency or temporal features. "7," recognized correctly in all 16 samples, exemplifies the model's strength in identifying acoustically distinct digits. On the other hand, the confusion matrix also reveals the challenge of separating digits with similar acoustic waveforms. For example, "3" is occasionally misclassified as "0" or "6," reflecting acoustic similarities between these digits. A cross-correlation analysis supports this: "3" and "6" have a correlation value of 5.9, reflecting close similarity, whereas "1" and "9" have a much lower value (−0.21), confirming clearer distinctions. Dataset composition can also influence overall accuracy: overrepresenting challenging digits, such as "3" and "6," may yield lower accuracy, whereas a more balanced distribution may yield higher accuracy. We therefore adopt a balanced dataset, where each digit is uniformly represented to ensure fair evaluation. These findings reveal both the strengths and limitations of our approach. Achieving 89% accuracy with a single physical node time-multiplexed into ten virtual nodes demonstrates the system's efficiency and the potential for utilizing transient PMC dynamics. However, performance on acoustically similar digits may be improved by refining preprocessing steps or more advanced training algorithms.

Figure 6 presents how classification accuracy depends on two key parameter variations in our time-multiplexed reservoir. Figure 6a plots classification accuracy against the input pulse interval δ with node count $N = 10$. At $\delta = 1$ ns, output pulses can overlap substantially, enabling stronger inter-node connections and achieving nearly 90% accuracy. As δ increases to 5 ns, accuracy drops to roughly 80%, indicating that a weaker overlap degrades the reservoir's performance. Because $\Delta\tau$ must be short enough to keep $\tau = 10 \times \Delta\tau$ (ns) below 40 ns, lengthening δ too much reduces both nonlinearity and memory in the transient regime.

Figure 6b shows results when N varies at $\delta = 1.0$, 1.5, 2.5, and 3.5 ns, exploring how dimensionality and pulse spacing together affect accuracy. In this system, the virtual node interval $\Delta\tau$ comprises both δ and a fixed 3 ns pulse width (limited by our instrumentation), while the total delay τ is given by $\tau = N \times \Delta\tau$. Through experimental validation, we established an optimal threshold value of $\tau = 40$ ns (which turns out to be approximately the cavity magnon-polariton decay time τ_{CMP}), by employing 10 nodes and 4.0 ns interval per node, balancing between node connectivity and signal retention.

In detail, with a moderate node count ($N \approx 10$) and relatively small δ, the system attains ~90% accuracy. Fewer than $N = 8$ nodes result in insufficient dimensionality, while more than $N = 15$ yields redundancy or overfitting at short intervals. Beyond that range, additional nodes do not significantly enhance performance, indicating the reservoir already captures the input signal. For $\delta = 1.0$ ns and $N = 40$, accuracy drops to 78% as the reservoir becomes overly sensitive to small input fluctuations, amplifying noise in a high-dimensional space. In contrast, at larger intervals ($\delta = 2.5$ or 3.5 ns), pulses do not overlap enough to create correlated states, leading to comparatively low accuracy[5]. Testing beyond $N = 15$ at $\delta = 3.5$ ns was prohibited due to computer memory constraints.

From these results, three practical conditions emerge: (1) δ must remain short enough to enable overlapping oscillations and robust inter-node coupling; (2) N should be chosen to avoid both insufficient dimensionality (two few nodes) and excessive redundancy (too many); and (3) $\tau = N \times \Delta\tau$ should stay well below the decay time (~40 ns) to prevent the transient amplitude from fading prematurely, thus implementing a short-term memory. When all these conditions are satisfied, the time-multiplexed reservoir can fully utilize the nonlinear characteristics of PMC, thereby supporting high performance in tasks such as spoken digit recognition.

Discussion

We establish a physical RC approach that utilizes the transient dynamics of PMC with a single-physical-node architecture, effectively producing multiple virtual nodes through time multiplexing. By harnessing the system's transient response, we show that the intrinsic nonlinear behavior in a strong PMC regime can efficiently handle complex temporal tasks. Our experiments confirm that transient PMC behavior enables high-dimensional computational states, achieving ~89% accuracy in spoken-digit recognition with only ten nodes, which represents a substantial reduction in hardware compared to traditional RC systems that often require hundreds or thousands of nodes.

Performances are affected by the ratio between the total sampling duration τ and the cavity magnon-polariton decay time τ_{CMP}. For instance, $\Delta\tau = 4$ ns and $N = 10$ ($\tau = 40$ ns $= \tau_{CMP}$) produced optimal results, preserving oscillation amplitude near 1 V. If $\Delta\tau$ is too short, the system underfits, missing critical temporal features. Conversely, when τ surpasses τ_{CMP} due to an excessive number of nodes, the weakened feedback disrupts sequential information retention, potentially resulting in overfitting rather than improved accuracy. By maintaining an optimal $\Delta\tau$ - N combination, the intrinsic short-term memory from PMC is fully exploited, enabling strong temporal correlations and memory capacity with minimal hardware.

To benchmark our PMC-based RC against other spintronic RC approaches, we compared several state-of-the-art implementations in Table 1. While other spin-based systems, such as spin-torque nano-oscillators and magnetic skyrmion-based reservoir computing, achieve accuracies ranging from 85% to 99.6% using 16 to 500 nodes, our single-node system achieves comparable or higher accuracy with far fewer nodes, demonstrating the effectiveness of transient dynamics in a strong PMC regime. For example, phonon-magnon coupling in waveguides achieves 91.4% accuracy with 11 nodes[20], suggesting that strong coherent interactions between different excitations effectively enhance computing performance, independent of the

Table 1 | Comparison of various spintronic RC systems, detailing the components, computational approaches, target tasks, node counts, and achieved accuracies

Components	Algorithms	Number of nodes	Tasks	Accuracy	Reports
Photon-magnon hybrid system	Reservoir Computing	10	Spoken digit recognition	89%	Current work
GaAs/AlAs phonon waveguide	Reservoir Computing	11	Visual shape recognition	91.4%	20
Spin-torque nano-oscillator	Reservoir Computing	400	Spoken digit recognition	99.6%	24
(Ta/CoFeB/MgO) ×15 multilayer heterostructure	ANN	100	MNIST handwritten digit	89.5%	19
Magnetic skyrmion	Reservoir Computing	196	MNIST handwritten digit	87.6%	18
Skyrmion-spin wave	Reservoir Computing	353	MNIST handwritten digit	88.2%	46
Single micromechanical nonlinear resonator	Reservoir Computing	400	MNIST handwritten digit	93%	21
Spin wave	Reservoir Computing	196	MNIST handwritten digit	89.6%	47

The proposed PMC-based RC system achieves competitive accuracy with significantly fewer nodes, demonstrating its efficiency and potential for scalable, low-power neuromorphic applications.

specific coupling mechanism. Multilayer heterostructure ANN-based systems require 100 nodes for a similar level of accuracy[19]. Some designs, including a micromechanical resonator-based RC[21] reach 93% accuracy with 400 nodes, but our system shows superior hardware efficiency, making it particularly advantageous for low-power, compact devices. Although various reservoir computing schemes exist, as mentioned above, our PMC approach offers distinct advantages. Unlike photonic delay-line systems requiring meter-scale fiber propagation, our reservoir achieves temporal separation within a compact resonant structure, where fields are confined rather than distributed over long optical paths. Additionally, integrating bio-inspired pre-processing techniques such as cochlear filtering[24] could further improve discrimination between acoustically similar digits, potentially enhancing task accuracy.

Overall, our study bridges high computational performance and hardware efficiency, advancing practical, energy-conscious neuromorphic solutions for temporal data processing. Microwave pulses in our system function as transient excitation carriers that drive short-lived magnon-polariton responses for neuromorphic processing. A total of 500 input samples, each encoded as ten time-multiplexed pulses, were used: 400 for training and 100 for testing. The per-sample energy consumption was estimated at 5.4 nJ, yielding 2.7 μJ in total. The system is implemented using a single YIG film and an inverted SRR structure, forming a planar, compact device with potential for on-chip miniaturization. Although the reservoir output is currently computed externally from the acquired waveform, magnon transistor-based devices, known for their exceptionally low operating energy near 10^{-18} J, significantly below that of standard CMOS technology (~10^{-16} J)[44], may offer a path toward further energy reduction. By refining and scaling PMC-based architectures further, including their realization through integrated design circuits[45], we aim to validate their role as efficient, practical platforms for neuromorphic computing.

Methods

Sample Fabrication

Inverted Split Ring Resonators (ISRRs) were fabricated on an RF-10 laminate substrate (with a relative permittivity of 10). A copper ground plane (thickness: 25 μm) was patterned using standard photolithography and etching techniques common in printed circuit board manufacturing. The substrate consisted of dielectric (0.64 mm thickness) and copper layers (0.035 mm thickness). The ISRRs dimensions were designed as follows: $a = 5$ mm, $b = 3.8$ mm, and $g = 0.4$ mm, as illustrated in Fig. 1a. Numerical simulations were performed in CST Microwave Studio to optimize the ISRR geometry. The microstrip line width was set to $w = 0.57$ mm to achieve a 50 Ω impedance, as determined using APPCAD software. The (111) oriented YIG thin films, 25 μm thick, were grown by liquid-phase epitaxy on Gadolinium Gallium Garnet (GGG) substrates and cut to lateral dimensions of 3.7×3.7 mm^2.

Measurement of Transient Response

To generate the pulsed RF signal, a Tektronix AFG 3242 arbitrary function generator and a Keysight E8257D RF signal generator were employed. The outputs were combined using a Pasternack PE44206 RF mixer to produce the input RF wave packet. In addition, to ensure sufficient RF power for the experiment, the signal from the mixer was amplified using an Ophir 5193E RF amplifier prior to injection into the system. The mixing process produces a different frequency $f_{\mathrm{mix}} = |f_{RF} - f_{LO}|$ where f_{mix} represents the mixed signal frequency, f_{RF} is the RF signal frequency, and f_{LO} is the local oscillator frequency. Since $f_{RF} \gg f_{LO}$. the mixed signal frequency is approximately 3.20 GHz.

The mixed signal was transmitted via a 50 Ω SMA connector to minimize signal loss and reflection before entering the PMC hybrid system composed of the ISRR and YIG components. An external magnetic field was applied across the YIG thin film using an electromagnet, allowing fine-tuning of the system's dynamic behavior. The transient response of the hybrid system was measured using a Keysight DSO91304A oscilloscope 13 GHz resolution, up to 40 GSa/s sampling rate. The DC magnetic field was oriented at an angle of $\phi = 33°$ relative to the x-axis (perpendicular to the microstrip line) to ensure selective excitation of the ferromagnetic resonance (FMR) mode, thus avoiding higher-order spin wave modes with non-zero wave numbers[14].

Computational Analysis Framework

We employed a time-multiplexed reservoir computing framework using a single physical node expanded into virtual nodes via time multiplexing. The system's internal dynamics, driven by photon–magnon coupling, generate nonlinear and temporally correlated reservoir states. The output is classified using SoftMax regression. The algorithmic details, including the reservoir architecture, feedback dynamics, and training procedure, are provided in Supplementary Sections S7–S9.

Data availability

Data supporting this study's findings are available from the corresponding author upon reasonable request.

Received: 17 December 2024; Accepted: 1 June 2025;
Published online: 30 June 2025

References

1. Indiveri, G. & Liu, S. C. Memory and information processing in neuromorphic systems. *Proc. IEEE* **103**, 1379–1397 (2015).
2. Markovic, D., Mizrahi, A., Querlioz, D. & Grollier, J. Physics for neuromorphic computing. *Nat. Rev. Phys.* **2**, 499–510 (2020).
3. Jaeger, H. & Haas, H. Harnessing nonlinearity: predicting chaotic systems and saving energy in wireless communication. *Science* **304**, 78–80 (2004).

4. Lukoševičius, M. & Jaeger, H. Reservoir computing approaches to recurrent neural network training. *Comput. Sci. Rev.* **3**, 127–149 (2009).
5. Appeltant, L., Soriano, M. C., Van der Sande, G., Danckaert, J. & Fischer, I. Information processing using a single dynamical node as complex system. *Nat. Commun.* **2**, 468 (2011).
6. Van der Sande, G., Brunner, D. & Soriano, M. C. Advances in photonic reservoir computing. *Nanophotonics* **6**, 561–576 (2017).
7. Brunner, D., Soriano, M. C. & Van der Sande, G. Photonic reservoir computing. *Nanophotonics* **8**, 19–20 (2019).
8. Vandoorne, K. et al. Toward optical signal processing using photonic reservoir computing. *Opt. Express* **16**, 11182–11192 (2008).
9. Larger, L. et al. High-speed photonic reservoir computing using a time-delay-based architecture: million words per second classification. *Phys. Rev. X* **7**, 011015 (2017).
10. Hülser, T., Köster, F., Jaurigue, L. & Lüdge, K. Role of delay-times in delay-based photonic reservoir computing. *Opt. Mater. Express* **12**, 1214–1231 (2022).
11. Li, C. et al. Efficient and self-adaptive in-situ learning in multilayer memristor neural networks. *Nat. Commun.* **9**, 2385 (2018).
12. Du, C. et al. Reservoir computing using dynamic memristors for temporal information processing. *Nat. Commun.* **8**, 2204 (2017).
13. Moon, J. et al. Temporal data classification and forecasting using a memristor-based reservoir computing system. *Nat. Electron.* **2**, 480–487 (2019).
14. Zhong, Y. et al. A memristor-based analogue reservoir computing system for real-time and power-efficient signal processing. *Nat. Electron.* **5**, 672–681 (2022).
15. Zhong, Y. Dynamic memristor-based reservoir computing for high-efficiency temporal signal processing. *Nat. Commun.* **12**, 408 (2021).
16. Yang, J. et al. Tunable synaptic characteristics of a Ti/TiO_2/Si memory device for reservoir computing. *ACS Appl. Mater. Interfaces* **13**, 33244–33252 (2021).
17. Tanaka, G. et al. Recent advances in physical reservoir computing: a review. *Neural Netw.* **115**, 100–123 (2019).
18. Jiang, W. et al. Physical reservoir computing using magnetic skyrmion memristor and spin torque nano-oscillator. *Appl. Phys. Lett.* **115**, 192403 (2019).
19. Lone, A. H. et al. Anomalous Hall and skyrmion topological Hall resistivity in magnetic heterostructures for the neuromorphic computing applications. *npj Spintronics* **2**, 3 (2024).
20. Yaremkevich, D. D. et al. On-chip phonon–magnon reservoir for neuromorphic computing. *Nat. Commun.* **14**, 8296 (2023).
21. Sun, J., Matsubara, M., Nagasaka, Y., Ono, T. & Yamaguchi, H. Novel nondelay-based reservoir computing with a single micromechanical nonlinear resonator for high-efficiency information processing. *Microsyst. Nanoeng.* **7**, 83 (2021).
22. Nakane, R., Hirose, A. & Tanaka, G. Spin waves propagating through a stripe magnetic domain structure and their applications to reservoir computing. *Phys. Rev. Res.* **3**, 033243 (2021).
23. Riou, M. et al. Neuromorphic computing through time-multiplexing with a spin-torque nano-oscillator. In *2017 IEEE International Electron Devices Meeting (IEDM)*, 36.3.1–36.3.4 (IEEE, 2017).
24. Torrejon, J. et al. Neuromorphic computing with nanoscale spintronic oscillators. *Nature* **547**, 428–431 (2017).
25. Pinna, D., Bourianoff, G. & Everschor-Sitte, K. Reservoir computing with random skyrmion textures. *Phys. Rev. Appl.* **14**, 054020 (2020).
26. Zhang, X. F., Zou, C. L., Jiang, L. & Tang, H. X. Strongly coupled magnons and cavity microwave photons. *Phys. Rev. Lett.* **113**, 156401 (2014).
27. Tabuchi, Y. et al. Coherent coupling between a ferromagnetic magnon and a superconducting qubit. *Science* **349**, 405–408 (2015).
28. Millet, L., Jeon, H., Kim, B., Bhoi, B. & Kim, S. K. Reservoir computing using photon-magnon coupling. *Appl. Phys. Lett.* **119**, 182405 (2021).
29. Match, C., Harder, M., Bai, L. H., Hyde, P. & Hu, C. M. Transient response of the cavity magnon-polariton. *Phys. Rev. B* **99**, 134445 (2019).
30. Wolz, T. et al. Introducing coherent time control to cavity magnon–polariton modes. *Commun. Phys.* **3**, 3 (2020).
31. Nakajima, K. & Fischer, I. *Reservoir Computing* (Springer, 2021).
32. Schumacher, J., Toutounji, H. & Pipa, G. in *Artificial Neural Networks and Machine Learning ICANN 2013: 23rd International Conference on Artificial Neural Networks Sofia, Bulgaria. Proceedings* 23, 26–33 (Springer, 2013).
33. Escalona-Morán, M. A., Soriano, M. C., Fischer, I. & Mirasso, C. R. Electrocardiogram classification using reservoir computing with logistic regression. *IEEE J. Biomed. Health Inform.* **19**, 892–898 (2015).
34. McDonnell, A. C. & Trefzer, M. A. The effect of system timescale on virtual node connectivity within delay-feedback reservoirs. In *Proc. Int. Jt. Conf. Neural Netw. (IJCNN),* Gold Coast, Australia, 1-8 (IEEE, 2023).
35. Bhoi, B., Kim, B., Kim, J., Cho, Y. J. & Kim, S. K. Robust magnon-photon coupling in a planar-geometry hybrid of inverted split-ring resonator and YIG film. *Sci. Rep.* **7**, 11930 (2017).
36. Kim, B., Bhoi, B. & Kim, S. K. Spin-wave excitation and critical angles in a hybrid photon-magnon-coupled system. *J. Appl. Phys.* **126**, 163902 (2019).
37. Harder, M. & Hu, C. M. Cavity spintronics: an early review of recent progress in the study of magnon-photon level repulsion. *Solid State Phys.* **69**, 47–121 (2018).
38. Nakajima, K., Hauser, H., Li, T. & Pfeifer, R. Exploiting the dynamics of soft materials for machine learning. *Soft Robot.* **5**, 339–347 (2018).
39. Jackson, Z. Free spoken digit dataset. https://github.com/Jakobovski/free-spoken-digit-dataset (2016).
40. Cucchi, M., Abreu, S., Ciccone, G., Brunner, D. & Kleemann, H. Hands-on reservoir computing: a tutorial for practical implementation. *Neuromorph. Comput. Eng.* **2**, 032002 (2022).
41. Hosmer Jr, D. W., Lemeshow, S. & Sturdivant, R. X. *Applied Logistic Regression* (John Wiley & Sons, 2013).
42. Dietterich, T. Overfitting and undercomputing in machine learning. *ACM Comput. Surv.* **27**, 326–327 (1995).
43. Hawkins, D. M. The problem of overfitting. *J. Chem. Inf. Comput. Sci.* **44**, 1–12 (2004).
44. Chumak, A., Serga, A. & Hillebrands, B. Magnon transistor for all-magnon data processing. *Nat. Commun.* **5**, 4700 (2014).
45. Li, Y. et al. Strong coupling between magnons and microwave photons in on-chip ferromagnet–superconductor thin-film devices. *Phys. Rev. Lett.* **123**, 107701 (2019).
46. Lee, M.-K. & Mochizuki, M. Handwritten digit recognition by spin waves in a Skyrmion reservoir. *Sci. Rep.* **13**, 19423 (2023).
47. Namiki, W. et al. Experimental demonstration of high-performance physical reservoir computing with nonlinear interfered spin wave multidetection. *Adv. Intell. Syst.* **5**, 2300228 (2023).

Acknowledgements

This work was supported by the National Research Foundation of Korea (NRF) grant funded by the Korea government (MSIT) (No. RS-2024-00347921).

Author contributions

S.-K.K., H.-C.J. and L.M. conceived the main idea and designed the experiments. H.-C.J. and B.-J.K. contributed to the instrumental setup and performed the measurements. H.-C.J. and L.M. analyzed the data. S.-K.K. supervised the work. All the authors equally contribute to write the manuscript.

Competing interests
The authors declare no competing interests.

Additional information
Supplementary information The online version contains supplementary material available at https://doi.org/10.1038/s44306-025-00092-1.

Correspondence and requests for materials should be addressed to Sang-Koog Kim.